Nanoparticles-loaded plastic scintillators for fast/thermal neutrons/gamma discrimination: Simulation and results

Camille Frangville, Amélie Grabowski, Jonathan Dumazert, Eva Montbarbon, Clément Lynde, Romain Coulon, Amélie Venerosy, Guillaume Bertrand, Matthieu Hamel

Nanoparticles-loaded plastic scintillators for fast/thermal neutrons/gamma discrimination: simulation and results

Camille Frangville[1], Amélie Grabowski[1], Jonathan Dumazert[1*], Eva Montbarbon[1], Clément Lynde[1], Romain Coulon[1], Amélie Venerosy[2], Guillaume H. V. Bertrand[1], Matthieu Hamel[1*]

[1] CEA, LIST, Laboratoire Capteurs et Architectures Électroniques, F-91191 Gif-sur-Yvette, France.

[2] CEA, LIST, Laboratoire Capteurs Diamant, F-91191 Gif-sur-Yvette, France.

*Correspondence to: jonathan.dumazert@cea.fr and matthieu.hamel@cea.fr.

Abstract

We report herein the application of a new series of plastic scintillators loaded with lithium tetraborate nanoparticles ($Li_2B_4O_7$) designed for the simultaneous detection of fast neutrons, thermal neutrons and gamma. First, MCNP simulations are performed to highlight the potential benefit of $Li_2B_4O_7$ loading. Then, a nanoparticle-loaded scintillator is prepared and evaluated towards the detection of a partially thermalized neutron/gamma 252-californium source. Several scenarios of radiation/matter interactions are evaluated against the observed results. A detection chamber composed of boron-containing chipboard wood has been specifically designed and a subtraction method was set up to afford the best discrimination pattern. For the first time, a triple discrimination is presented with a nanoparticles-loaded plastic scintillator, where both $^{6}Li(n,\alpha)$ and $^{10}B(n,\alpha)$ signatures are observed. A Figure of Merit of 1.40 was calculated between fast neutrons and gamma rays around 480 keVee. The Figure of Merit between fast + thermal neutrons and gamma rays is slightly worse as it is 1.16 at 380 keVee.

Keywords

Plastic scintillators; nanoparticles; thermal neutrons; fast neutrons; discrimination

1. Introduction

Detection of special nuclear materials (SNMs – mainly ^{233}uranium, ^{235}uranium and ^{239}plutonium) constitutes a major effort in the field of Homeland Security. For a long time, ^{3}He based detectors were considered as the gold standard in terms of neutron detection that can reveal the trafficking of such SNMs. However, the 2010's have seen a revival in terms of chemical modifications of plastic scintillators generally speaking,[1] and specifically tuned for this application.[2] The spontaneous fission of materials such as SNMs sees the release of fast neutrons whose kinetic energy is distributed with a Watt spectrum with an average energy around 2 MeV. These neutrons may slow down through multiple scatterings with their surroundings, leading to neutrons with much lower energy, falling down to the thermal energy

equal to 25 meV at 300 K. Thus, one can admit that a sufficiently shielded SNM with moderating materials such as polyethylene may only been "seen" as a low-energy neutron emitter. So, the larger the neutron energy range that is covered, the more versatile and efficient the sensor will be.

Detecting thermal neutrons with plastic scintillators is usually performed by loading the material with neutron absorbing elements. Table 1 gives the comparison between the main elements that are able to create a nuclear reaction of interest with thermal neutrons. ^{10}B loaded plastic scintillators are probably the most studied and they are even commercially available from several suppliers for decades. To the best of our knowledge, the first boron-loaded organic scintillator was liquid, and trimethyl borate ($B(OCH_3)_3$) was the boron source used in the formulation.[3] Now, most of the research cited in the literature advocates the use of lithium, boron[2] or even gadolinium.[4] Li and B may have both pros and cons in their use, but they do operate in almost the same way, since the created ions (alpha, triton and Li^{3+} particles) represent the thermal neutron signature and display different pulse shapes from gamma interactions. Even at the natural isotopic loading, Gd displays the highest cross section for capturing thermal neutrons (254,000 barns), but the interaction releases gamma-rays that makes it inadequate for pulse shape discrimination. In that case, a compensation or coincidence scheme can be successfully applied.[5]

Table 1. Typical thermal neutron absorptions.

Isotope	Thermal neutron capture reaction	25 meV cross section (Barns)	Natural isotopic abundance (%)
^{3}He	$^{3}_{2}He + n \rightarrow {}^{3}_{1}H + {}^{1}_{1}p$	5330	0.000137
^{6}Li	$^{6}Li + n \rightarrow {}^{3}H\ (2.73\ MeV) + \alpha\ (2.05\ MeV)$	940	7.5
^{10}B	$^{10}B + n \rightarrow {}^{7}Li^{*} + \alpha\ (1.47\ MeV) \rightarrow {}^{7}Li + \alpha\ (1.8\ MeV) + \gamma\ (0.48\ MeV)$	3840	19.9
^{113}Cd	$^{113}Cd + n \rightarrow {}^{114}Cd + \gamma's\ (9\ MeV)$	20600	12.2
^{155}Gd	$^{155,157}Gd + n \rightarrow {}^{156,158}Gd* \rightarrow {}^{156,158}Gd + e^{-} + \gamma's\ (8\ MeV)$	60900	14.7
^{157}Gd		254000	15.7

Loading plastics with lithium is particularly challenging. Indeed, it is worth mentioning the issues encountered when loading apolar, scintillating polymers (typically polystyrene or poly(vinyltoluene)) with polar elements such as the lithium salt. Among the different available solutions, lithium nanoparticles (NPs) are particularly advantageous. Loading nanoparticles in plastic scintillators is an emerging field, both for gamma spectrometry[6] and for thermal neutron counting. For the latter purpose, this was already shown by Carturan *et al*. who dispersed oleic-capped lithium fluoride nanocrystals in a polysiloxane matrix.[7,8,9]

Based on this strategy, we present our results regarding chemical modifications of plastic scintillators, firstly with a high concentration of primary fluorophore for the detection of fast neutrons. It is now well known that materials may present pulse shape discrimination (PSD) properties thanks to the difference between delayed and prompt fluorescence,[2] and two of them are currently commercially available from Eljen Technology and Amcrys. Secondly, by

adding not only lithium NPs, but also a mixture of lithium and boron, namely in the form of lithium tetraborate $Li_2B_4O_7$, we take advantage of these two neutron absorbers to largely increase thermal neutron capture efficiency. In the field of radiation detection, lithium tetraborate is already known as a tissue equivalent thermoluminescent, gamma-ray dosimeter.[10] However, to the best of our knowledge, scintillators loaded with a mixture of two or more neutron absorbers are poorly studied.[11,12] From this combination, we expect a counting sensitivity improvement of both fast and thermal neutrons, especially in the case where small sensors are used such as in hand-held devices.

Thus, the first section presents the MCNP6.1 simulation, which supports our motivation and theory. This simulation allows us to determine the trend of the response of a homogenously loaded plastic scintillator with $Li_2B_4O_7$ NPs. It shows that for a 10-cm^3 size sample, starting with 0.1 weight percent (wt%) loading may already give a relevant capture rate which could be detected. Then the fast and thermal neutron/gamma discrimination is evaluated by exposing the NP-loaded plastic scintillator to a partially thermalized 252-californium radioactive source, used as a SNM laboratory surrogate. To confirm all the nuclear processes occurring in the material, several hypotheses were formulated. A boron-containing chipboard wood cage was built and a PSD subtraction method was designed which highlights the signature of up four different interactions: gamma and fast neutrons are easily separated by PSD, and two extra features – corresponding to thermal neutron capture by lithium and boron – appear as well.

2. Experimental section

The synthesis of our material is reported elsewhere.[13] 0.3 wt% of fully enriched $^6Li_2{}^{10}B_4O_7$ NPs were added to an argon-saturated solution of monomers containing PPO (20 wt%) and POPOP (0.03 wt%). No initiator has been used. 5 cycles of degassing under vacuum were performed then the mixture was poured in a glass jar and sealed under argon atmosphere and cured between 60 – 110 °C for 10 to 15 days. After complete polymerization, the mold was shattered and the free piece was cut and polished until obtaining an optical-grade surface. Ultimately, the scintillator was covered with Teflon® tape to optimize optical focalization towards the photomultiplier tube, thereby allowing gamma spectra and n/γ discrimination experiments. The diameter of the scintillator is 32 mm and the thickness 11 mm, weight 9.64 g, density 1.09.

EJ-200 plastic scintillator was obtained from Eljen Technology.

Gamma-ray spectra were recorded as follows: the sample was optically coupled with RTV141A optical grease to a Hamamatsu R7724-100 photomultiplier. A 387-kBq ^{60}Co source was used to excite the material. Two experimental series were performed: one with the prepared plastic scintillator and the other with a commercial sample of same size. Pulses coming from the PMT were sorted and treated with a custom-made electronic board. The high voltage was kept constant during both experiments, using a stabilized high voltage module N1470 from CAEN. The Compton edge (CE) was fitted with a Gaussian function and the accurate determination of the Compton edge position was evaluated at 80 % of the decrease of this

Gaussian shape. By rule of thumb, the light yield of the prepared plastic scintillator sample could be determined from the commercial data sheet (herein 10,000 ph/MeV for EJ-200 plastic scintillator):

$$R_{sample} = R_{EJ-200} \times V_{CE,sample}/V_{CE,EJ-200}$$

where *R* is the light yield, and *V* is the channel of the Compton edge position.

In order to assess its neutron/gamma discrimination ability, the scintillator was coupled using RTV141A optical grease to a Hamamatsu H11284MOD photomultiplier tube fed with a CAEN N1470 high voltage operating in negative mode. The {scintillator + PMT} system was placed 15 cm away from a ^{252}Cf source (≈ 1.8 MBq activity), the latter being partially thermalized with a 10 cm thick polyethylene brick. To reduce the gamma-ray incident flux on the sample, a 5 cm denal® brick (a tungsten-based alloy) was added between the ^{252}Cf source and the polyethylene brick. The anode signal fed a CAEN DT5730B digitizer, running with the DPP-PSD software. Scintillation pulses were then recorded and post-processed using a charge-comparison method.[14] The Figure of Merit was finally calculated; it is a standard factor for the evaluation of the n/γ discrimination power and has already been fully referenced.[2] Along with this experiment and with the strictly same setup, an energy calibration was performed with a 530 kBq ^{137}Cs source. The quality of the PSD was quantitatively estimated from the calculation of the Figure of Merit (FoM), which has the following formula:

$$FoM = \frac{\left|\mu_n - \mu_\gamma\right|}{2.35(\sigma_n^2 + \sigma_\gamma^2)}$$

where μ_n and μ_γ are the mean values of the neutron and the gamma ray peaks, and σ_n and σ_γ are the standard deviations of neutron and gamma distributions fitted with Gaussian functions $\mathcal{N}(\mu_n, \sigma_n)$ and $\mathcal{N}(\mu_\gamma, \sigma_\gamma)$.

3. Results

3.1. Simulation of the spectral signature and capture rate of thermal neutron radiations in $Li_2B_4O_7$ loaded plastic scintillator

The addition of both boron and lithium is firstly motivated by the fact that these elements ultimately release energetic and charged particles after the capture of a slow neutron. The nuclear reactions underlying the emission of these products are:

- the $^{10}\mathrm{B}(\mathrm{n}, \alpha)$ absorption reaction: thermal neutrons are absorbed by boron-10 nuclides, which is of natural abundance close to 20 %. Following the absorption, the nucleus disintegrates following Eq. (A) with a 6 % probability, and following Eq. (B) with a 94 % probability, owing that the produced lithium-7 nucleus is found in its fundamental or excited state.

$$^{10}_{5}\mathrm{B} + ^{1}_{0}\mathrm{n} \rightarrow {}^{7}_{3}\mathrm{Li} + {}^{4}_{2}\mathrm{He} \quad (\mathrm{A})$$

$$^{10}_{5}\mathrm{B} + ^{1}_{0}\mathrm{n} \rightarrow {}^{7}_{3}\mathrm{Li}^{*} + {}^{4}_{2}\mathrm{He} \quad (\mathrm{B})$$

The associated cross section at $E_{th} = 25$ meV is $\sigma_{E_{th}} = 3840$ b and the Q values are 2.31 MeV and 2.79 MeV for Eq. (A) and (B) respectively. The said Q value is shared between a lithium-7 nucleus and an alpha particle, with respective kinetic energies $E_{^7_3\mathrm{Li}} = 0.84$ MeV, and $E_\alpha = 1.47$ MeV. From Eq. (B), a 0.48 MeV gamma ray is also released following the de-excitation of lithium-7.

- the $^6\mathrm{Li}(\mathrm{n},\alpha)$ absorption reaction: thermal neutrons are absorbed by lithium-6 nuclides (7.5 % natural abundance), according to Eq. (C).

$$^6_3\mathrm{Li} + ^1_0\mathrm{n} \rightarrow {}^3_1\mathrm{H} + {}^4_2\mathrm{He} \quad (\mathrm{C})$$

The associated cross section is $\sigma_{E_{th}} = 940$ b with a Q value of 4.78 MeV, that is shared between a tritium and an alpha particles with respective kinetic energies $E_{^3\mathrm{H}} = 2.73$ MeV, and $E_\alpha = 2.05$ MeV.

Aside the two (n,α) absorption reactions from the embedded nanoparticles, we should mention (n,γ) capture reactions occurring inside the polymer matrix, with microscopic cross sections ranging from the order of 0.1 mb up the order of 100 mb. However, due to the small volume of the scintillator (about 9 cm^3), the macroscopic cross section for (n,γ) reactions, as well as the photoelectric and Compton interaction yield of the high-energy gamma rays released after H, C, N, O capture, are expected to be too low for practical use. We shall discuss this assumption in the rest of the analysis.

A modeling study, using the MCNP6.1 particle transport software package[15] was conducted to simulate the response of the plastic scintillator loaded with lithium tetraborate nanoparticles. The aim of this Monte-Carlo study is to provide a description of the response trend of the sensor when confronted to 25 meV, thermalized neutrons. The neutron source is considered homogenous and isotropic, surrounding the sensor. The key parameter appears to be the nanoparticle loading weight.

Let us consider a cross-linked plastic scintillator with a suitable composition for fast neutron/gamma discrimination.[16] The density $\rho_m = 1.07\ \mathrm{g.cm^{-3}}$, and the elemental composition (C, H, N, O) are injected into the code. The embedded crystals are of composition $Li_2B_4O_7$. The scintillator medium was modeled according to the dimensions of the synthetized samples that are experimentally studied in the following section, *i.e.* 1.6-cm-radius by 1.1-cm-height in a perfect cylindrical shape. As we used a homogenous spherical neutron source in the model, it thus follows that the plastic thickness in neutron direction is in the order of 1 cm. In a first-order-approximation, we consider their insertion of the elements forming these nanocrystals to be homogenous inside the polymer matrix.

The output estimates of interest in view of simulation-based, design study are:

- the neutron absorption yield within the scintillator, thereafter noted as τ_a and homogenous to a number of captures per source neutron (n^{-1});
- the energy deposition yield per source neutron inside the scintillator, induced by secondary particles that are released after (n,α) and (n,γ) capture reactions. This yield is

a function of energy E and is labeled $\tau_D(E)$. We express this estimate in energy deposition per source neutron, and per energy bin ($n^{-1}.keV^{-1}$).

The available kinetic energy from the capture reactions $\tau_D(E)$ allows us to separate the respective contributions of boron and lithium with respect to the thermal neutron-induced signal. It is worth mentioning that photoluminescence quenching was not considered in the simulation.

A quantitative analysis of the indirect neutron signature is carried out using the following concentrations: 0, 0.3, 0.5, 1, 3 and 5 wt% of nanoparticles. In all cases, the lithium tetraborate content is simulated in its 100 % isotopically enriched lithium and boron version, therefore $^{6}Li_2{}^{10}B_4O_7$. For the sake of explanation, we break down the overall neutron absorption yield τ_a in two terms: $\tau_a(\mathrm{n},\alpha)$ from $^{10}\mathrm{B}(\mathrm{n},\alpha)$ and $^{6}\mathrm{Li}(\mathrm{n},\alpha)$ reactions, and $\tau_a(\mathrm{n},\gamma)$ for the abovementioned capture reactions taking place inside the polymer matrix. The evolutions of estimated yields $\tau_a(\mathrm{n},\alpha)$ and $\tau_a(\mathrm{n},\gamma)$ according to the concentration of lithium tetraborate inside the scintillator are reproduced in Figure 1 below.

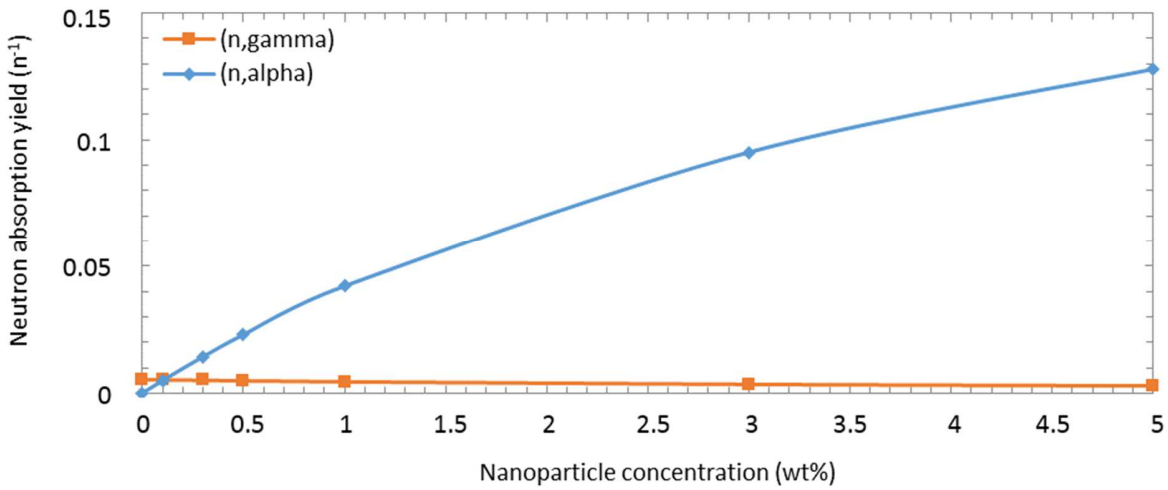

Figure 1. Neutron absorption yields $\tau_a(n,\alpha)$ and $\tau_a(n,\gamma)$ as a function of lithium tetraborate concentration within the plastic scintillator.

Figure 1 shows that, in terms of the total neutron absorption yield $\tau_a = \tau_a(\mathrm{n},\alpha) + \tau_a(\mathrm{n},\gamma)$, a gain by a factor of two is observed as soon as 0.1 wt% of nanoparticles are added, with a strong growth up to a homogenous concentration of 5 wt%. As far as the study of concept underlying this paper is concerned, we are trying to embed $Li_2B_4O_7$ with the lowest concentration (in order to ensure the highest possible scintillator light yield) that still ensures a significant increase of the neutron absorption yield. Now, the evolution curves show that, when adding 0.3 wt% of lithium tetraborate, a 350 % increase of τ_a compared to the unloaded equivalent scintillator is observed. We thus selected this initial load for the study of concept.

Because of the homogenous modeling of the loading, the estimated neutron yield is directly accounted for by sum of the values of $N \cdot \sigma_{E_{th}}$, N being the atomic density of a given

neutron absorber, and $\sigma_{E_{th}}$ the above-introduced cross section. Figure 1 illustrates the second motivation behind the choice of lithium-6 and boron-10 as neutron converters: a large microscopic cross section that compensates their relatively low atomic density even with such a low weight fraction as 0.3 wt%.

Now, our model will give accurate expectations of the performance of the lithium tetraborate-loaded scintillator scheme, provided that the charged (n,α) reaction products escape the nanoparticles with as low an energy loss inside $Li_2B_4O_7$ as possible, so that they remain spectrally identifiable. To assess the appropriateness of the size of the nanoparticles in our application, we estimated the stopping power S of lithium tetraborate, expressed in keV.µm^{-1}, for lithium ions at 0.84 MeV, alpha particles at 1.47 MeV and 2.05 MeV, and tritium (*i.e.* hydrogen) at 2.73 MeV. The estimation was carried out using the validated software package.[17] The values of S equal 626.9 keV.µm^{-1} for lithium ions at 0.84 MeV, 372.9 keV.µm^{-1} and 319.7 keV.µm^{-1} for alpha particles at 1.47 MeV and 2.05 MeV, and 26.2 keV.µm^{-1} for tritium at 2.73 MeV. Several NP syntheses were performed to afford them the smallest size, and our best method allowed us to isolate $Li_2B_4O_7$ NPs with an average size around 66 ± 22 nm. This batch was ultimately used for scintillator loading. Considering the most penalizing scenario of a reaction product generated on the surface of the nanoparticle, and having to cross the longest axis of the nanoparticle (herein most probably the NP diameter) before reaching the polymer matrix, the maximum range inside the lithium tetraborate is considered equal to 66 nm. It thus follows that a lithium ion of 0.84 MeV will lay down a maximum of 41.3 keV inside the nanoparticle (about 5 % of its initial energy), alpha particles of 1.47 MeV and 2.05 MeV maxima of 24.6 keV and 21.1 keV respectively (2 % and 1 %), and a tritium ion a maximum of 1.7 keV (less than 0.1 %). Such differences being far less than the expected energy resolution associated to the scintillator spectral response, we conclude that they will not affect the identification procedure, and therefore confirm that the size of the prepared nanoparticle is fully suitable with the application at hand.

The simulated kinetic energy deposition $\tau_D(E)$ inside a 0.3 wt%-loaded scintillator, obtained from the interaction model we described at the beginning of this paragraph is reproduced in Figure 2, where labels (A), (B) and (C) relate to the reaction equations stated at the beginning of this paragraph. The energy deposition spectrum is dominated by the contribution of the reaction products from Eq. (A), (B) and (C), with the full energy expositions of the three Q-values that were listed. We note that the summation of the energy yields at the Q-values:

$$\tau_D(2.31\ \mathrm{MeV}) + \tau_D(2.79\ \mathrm{MeV}) + \tau_D(4.78\ \mathrm{MeV}) = 1.42 \cdot 10^{-2}\ \mathrm{n}^{-1}$$

equals 99.3 % of the neutron capture yield $\tau_a(\mathrm{n},\alpha)$ at 0.3 wt% that was reported in Figure 1, which indicates that the charged reaction products are fully stopped by the polymer matrix and therefore contribute to the signal of interest. This validates the first motivation for the selection of lithium tetraborate as a dopant that we discussed above. Moreover, we observe that the ratio

$$\frac{\tau_D(2.79\ \mathrm{MeV})}{\tau_D(2.31\ \mathrm{MeV})} = \frac{8 \cdot 10^{-4}}{1.23 \cdot 10^{-2}} \sim 7\ \%$$

while, as we mentioned, the reaction process of Eq. (B) is 16 times more likely than the one of Eq. (A): this ratio indicates that the gamma ray at 0.48 MeV is very like to escape the scintillator and therefore does not significantly contribute to a distinct signature of $^{10}\mathrm{B}(\mathrm{n},\alpha)$ reactions from the one carried by the lithium-7 and alpha particle charged products. The same conclusion may be drawn for the electromagnetic products of (n,γ) captures, for which, as expected, the simulated spectrum shows no identifiable signature up to 10 MeV. Eventually, we see that

$$\frac{\tau_D(2.31\ \mathrm{MeV}) + \tau_D(2.79\ \mathrm{MeV})}{\tau_D(2.31\ \mathrm{MeV}) + \tau_D(2.79\ \mathrm{MeV}) + \tau_D(4.78\ \mathrm{MeV})} \sim 92\ \%$$

which corresponds to the ratios between the $N \cdot \sigma_{E_{th}}$ factors for boron-10 and lithium-6. In particular, it follows that boron-10 is expected to be the main contributor to the total alpha particle signature of neutron absorptions within the nanoparticle-loaded scintillator.

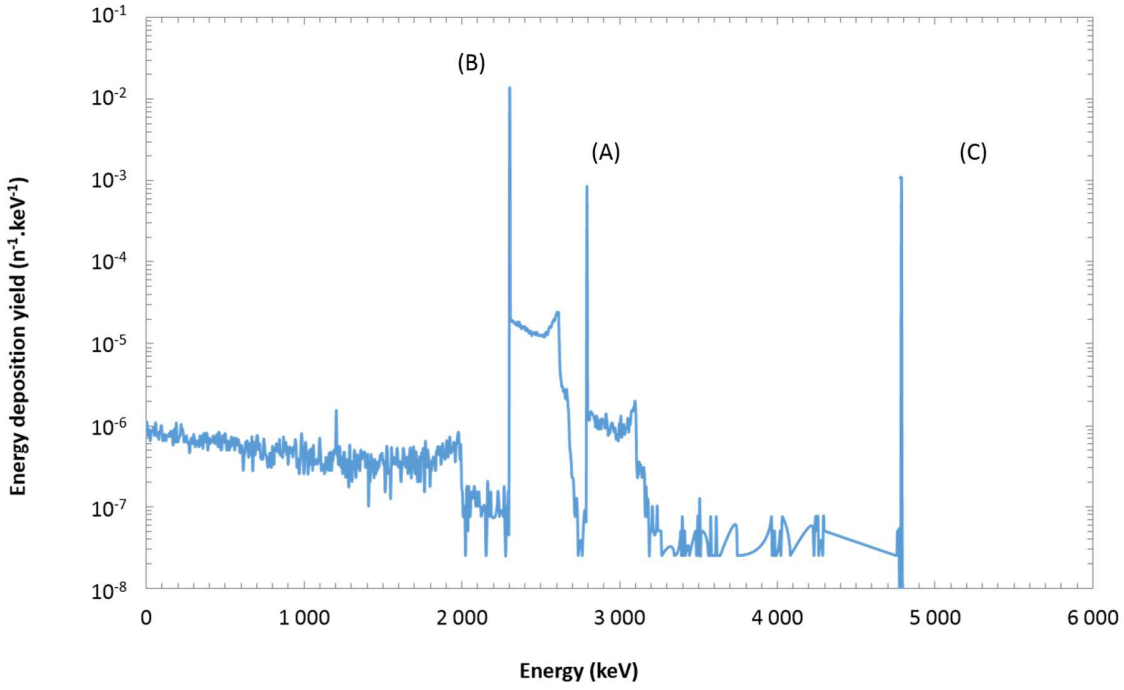

Figure 2. Available kinetic from reactions products of thermal neutron absorptions in a 0.3 wt% $Li_2B_4O_7$-loaded plastic scintillator. (A), (B) and (C) relate to the above-cited equations in the main text.

Let us mention, to conclude this paragraph, that the third motivation underlying our design is to use Pulse Shape Discrimination (PSD) as a tool for time-domain-based analysis. Such a processing ensures, in one single treatment, the discrimination of pulses emanating from gamma-rays, fast neutron interactions (explained above as delayed photoluminescence) and thermal neutrons (tritium, helium and lithium ions). In terms of signal characteristics, these particles are sorted from fastest to slowest pulse.[18] Therefore, a PSD method is adequate to

sort them into regions of interest inside a bi-parametric diagram, whose ideal pattern, as obtained after pulse classification, is depicted in Figure 3. When the abscissa gives the electron-equivalent energy laid down by interaction product, the ordinate represents the fraction between delayed charge against the total charge of a given pulse over a duration. The alpha quenching will be taken into consideration in the next section.

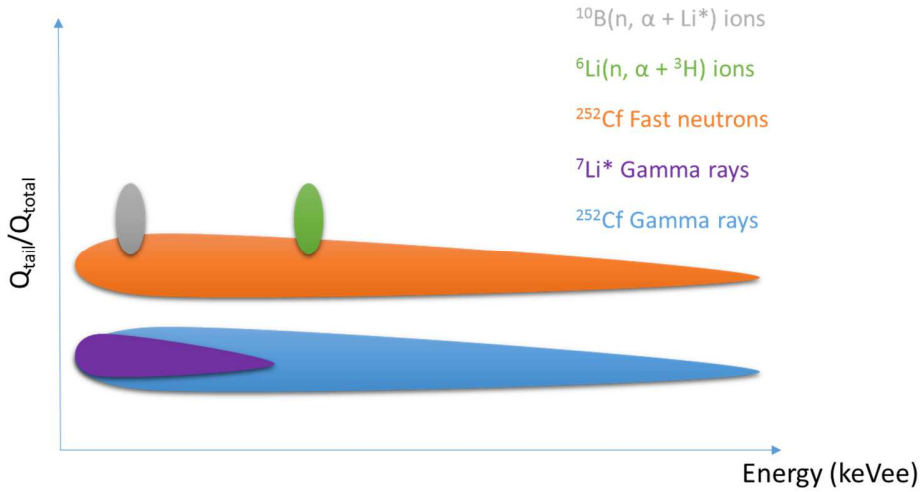

Figure 3. Idealized bi-parametric response of the NPs-loaded plastic scintillator to a partially moderated neutron source.

3.2. Preparation and characterization of the NP-loaded plastic scintillator

The preparation of the NP-loaded plastic scintillator has been described elsewhere.[13] It is noteworthy that the NPs are synthesized with the isotopes of interest, which are lithium-6 and boron-10. The photoluminescence data are representative of a scintillator with POPOP as the secondary fluorophore, giving an emission wavelength maximum close to 425 nm. $Li_2B_4O_7$ is expected to display a photoluminescence around 360 nm.[19] Under our experimental conditions, we did not notice any photoluminescence emanating from the nanoparticles. Falling under the absorption domain of POPOP, our hypothesis is that these photons may be reabsorbed by the secondary fluorophore. The transmission spectrum showed a strong absorption overall the visible domain, and as a result only 17 % of the light is transmitted at the maximum of emission of the scintillator. At the same wavelength, a reference EJ-200 plastic scintillator of same size and volume showed a 67 % transmission. A picture of the NP-loaded plastic and an EJ-200 sample is given Figure 4. A relative scintillation yield was measured against the same EJ-200 sample. ^{60}Co pulse height spectra were recorded with the same experimental setup, and the position of the Compton edges was compared according to the method described in the Experimental section. The relative scintillation yield was thus estimated around 3,750 ph/MeV.

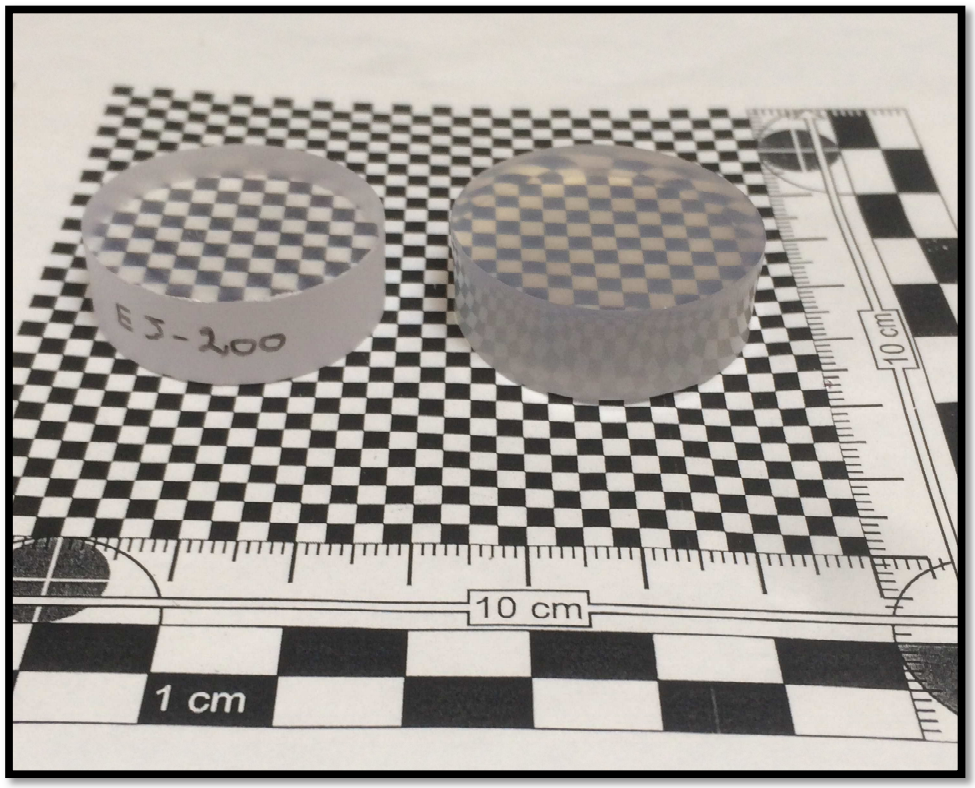

Figure 4. Picture of EJ-200 (left) and NP-loaded (right) plastic scintillators.

3.1. Neutron detection

The as-prepared plastic scintillator bearing isotopically enriched $^{6}Li_2{}^{10}B_4O_7$ nanoparticles was exposed to a partially polyethylene-thermalized 252-californium source. Thus, neutrons with various energies can interact within the scintillator, including 25 meV thermal neutrons. Figure 5 represents the energy-calibrated, pulse shape discrimination spectrum of the plastic scintillator. Three different regions of interest appear: the gamma plume at lower Q_{tail}/Q_{total} ratio, the fast neutron plume at higher Q_{tail}/Q_{total} ratio, and inside this fast neutron region an oval zone centered around 360 keVee that corresponds to thermal neutron capture reactions, as was explained in Figure 3. The calculated Figure of Merit value (FoM) around the Compton edge of ^{137}Cs (477 keVee) is 1.40. The FoM was also calculated for six different energy ranges, from low electron equivalent energy (230 keVee) up to 500 keVee, with a focus around the position of the alpha oval. It is noteworthy that the range that contains this oval displays a lower FoM, with a value of 1.15, whereas the surrounding FoM values are 1.21 and 1.36. This is explained by the broadening of the neutron-like pseudo-Gaussian shape, thus the increase of σ_n, which counts into the calculation of the FoM. On a side experiment, the NP-loaded plastic scintillator was benchmarked with two other plastics: its unloaded counterpart (hereafter designed as “regular”) and an EJ-276 commercial scintillator. The three scintillators displayed approximately the same volume within 18%. The calculated FoM values in the same energy range were 1.03, 1.26 and 1.79 for the NP-loaded, regular and EJ-276 plastic scintillators, respectively.

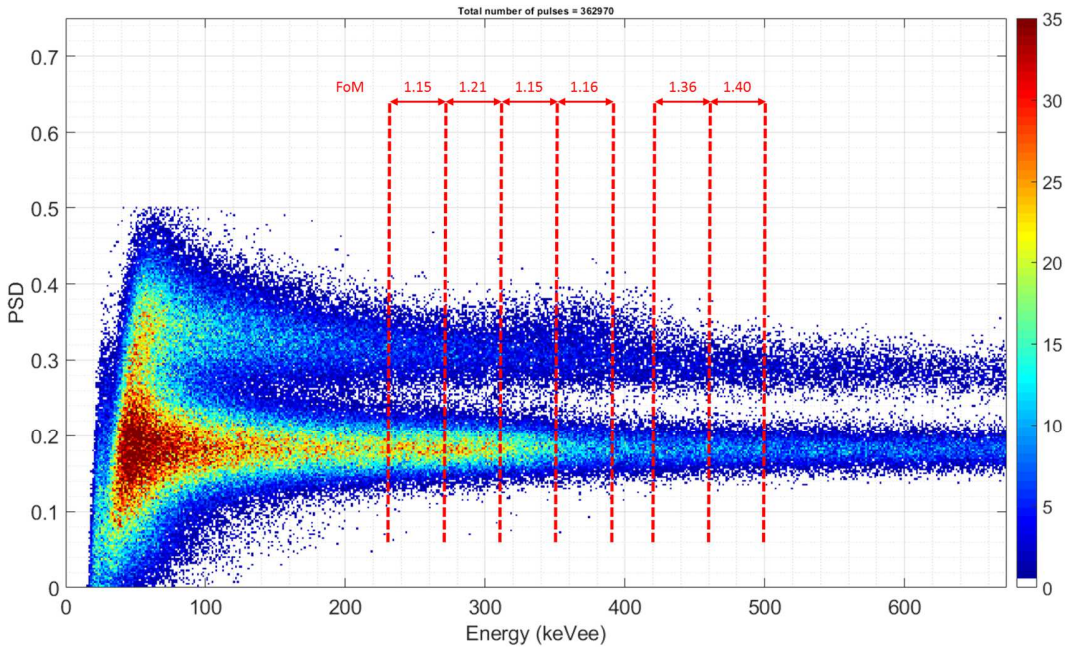

Figure 5. Neutron/gamma pulse shape discrimination pattern of the $^{6}Li_2{}^{10}B_4O_7$ nanoparticle-loaded plastic scintillator. A partially thermalized and shielded ^{252}Cf source was used for this experiment.

As a result of $Li_2B_4O_7$ loading, this ovoid signature between 300 and 420 keVee may be attributed to various reaction products:

a) Exclusive contribution of alpha from ^{6}Li (2.05 MeV);

b) Exclusive contribution of alpha from ^{10}B (1.47 MeV);

c) Exclusive contribution of triton from ^{6}Li (2.73 MeV);

d) Exclusive contribution of lithium ion from ^{10}B (0.84 MeV);

e) Combination of scenarios a) and b);

f) Exclusive contribution of the particles issued from ^{6}Li;

g) Exclusive contribution of the particles issued from ^{10}B;

h) Combination of scenarios f) and g).

The quenching factors occurring in plastic scintillators were then estimated. The Bethe formula gives: $(dE/dx) \propto z^2$ where z is the particle charge. The Birks formula gives $E_{ee}(E) \propto$

$L(E) \propto \int_0^E \frac{dE}{1+kB\left(\frac{dE}{dx}\right)} \approx \frac{E}{1+kB\varphi}$ with $\varphi \propto z^2$. So with important approximations $QF(E) = \frac{E_{ee}}{E} \propto \frac{1}{z^2}$, with QF being the quenching factor (in MeVee.MeV^{-1}).

Ref. 20 gives the quenching factor of recoil protons:

$$QF(E) = \frac{E_{ee}}{E} = \frac{0.034 \times E^2 + 0.125 \times E}{E}$$

The Bethe formula being independent from the particle's mass, we can thus consider the quenching factor of tritons somehow equal to that of the proton, so:

$$QF_T(2.73) \approx 0.218$$

For z = 2 (alphas), the quenching factor is estimated as

$$QF_\alpha(1{,}47) = \left(\frac{0.034 \times 1.47^2 + 0.125 \times 1.47}{1.47}\right)^2 \approx 0.031$$

$$QF_\alpha(2{,}05) = \left(\frac{0.034 \times 2.05^2 + 0.125 \times 2.05}{2.05}\right)^2 \approx 0.038$$

Based on the work of Mahl *et al.*,[21] we can estimate their quenching factor as 60/1470 = 0.041, which agrees with the order of magnitude of the calculated factor (formulation with PSD).

Finally, the same calculation for lithium ions (z = 3) gives a quenching factor

$$QF_{Li}(0.84) = \left(\frac{0.034 \times 0.84^2 + 0.125 \times 0.84}{0.84}\right)^3 \approx 0.0036$$

If these various quenching factors are reinjected into the different scenarios, we have:

a) A single signal centered around 0.038 × 2050 = 78 keVee;

b) A single signal centered around 0.031 × 1470 = 45 keVee;

c) A single signal centered around 0.218 × 2730 = 516 keVee;

d) A single signal centered around 0.0036 × 840 = 3 keVee;

e) A dual response giving an ovoid with two centers at 45 and 78 keVee;

f) A signal centered around 516 + 78 = 594 keVee;

g) A signal centered around 45 + 3 = 48 keVee;

h) A signal centered around 594 keVee and a signal around 48 keVee.

In conclusion, as far as orders of magnitude are considered, only scenarios c) and h) remain plausible. Consequently, the ovoid signal between 300 and 420 keVee differs from our rough calculations by a 30-to-50-% relative factor; we shall interpret this feature as being mainly attributable to the interaction between neutron-released tritons and the plastic medium.

Mahl *et al.* used a subtraction method to emphasize the thermal neutron capture in their design.[21] Thus, we completed our setup experiment in order to highlight the (n, α) reactions. A cage consisting of boron-loaded chipboard wood shielded on five edges the {scintillator + PMT} system. In a first experiment, the ^{252}Cf source was thermalized with 10 cm high density polyethylene (HDPE) and shielded with 5 cm of denal®. The second experiment was performed with the same strict experimental procedure except that HDPE was replaced by boron-loaded HDPE, the latter acting as thermal neutron poison, allowing therefore subtracting the thermal neutron captures we are interested in. This double experiment was performed twice at two different threshold values and the difference spectrum between these two experiments was computed. The results given in Figure 6 show the full bidimensional acquisition on the top and the neutron-associated region energy spectrum on the bottom. Again, the light ions oval located in the 350 keVee region remains visible but another pattern appears at lower energies, in the range 20 – 60 keVee. These counts are undoubtedly attributed to another neutron capture, but occurring now from the boron atom.

The sum of the counts S_{net} was calculated on these two regions (20 – 60 and 300 – 400 keVee), giving values of 2281 and 771 counts, respectively. The standard deviations Std(S_{net}) in the same regions were also calculated, giving values of 407 and 98, respectively. Thus we have: S_{net} = 5.6 × Std(S_{net}) in the range [20 – 60 keVee] and S_{net} = 7.9 × Std(S_{net}) in the range [300 – 400 keVee]. The comparison between S_{net} and Std(S_{net}) reveals that the signal isolated in these areas of interest is significant of the set of physical, neutron-related interactions we aimed at emphasizing in this experiment. Our material hence enables the distinct observation of four physical phenomena: gamma interaction, fast neutron interaction, thermal neutron capture by a ^{10}B nucleus and ultimately thermal neutron capture by a ^{6}Li nucleus.

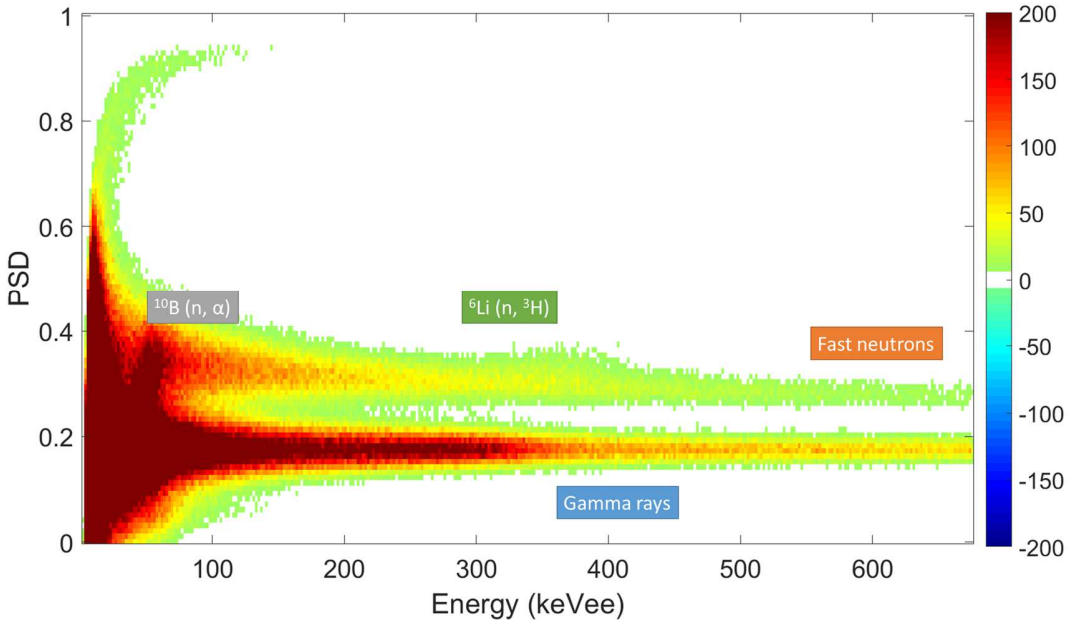

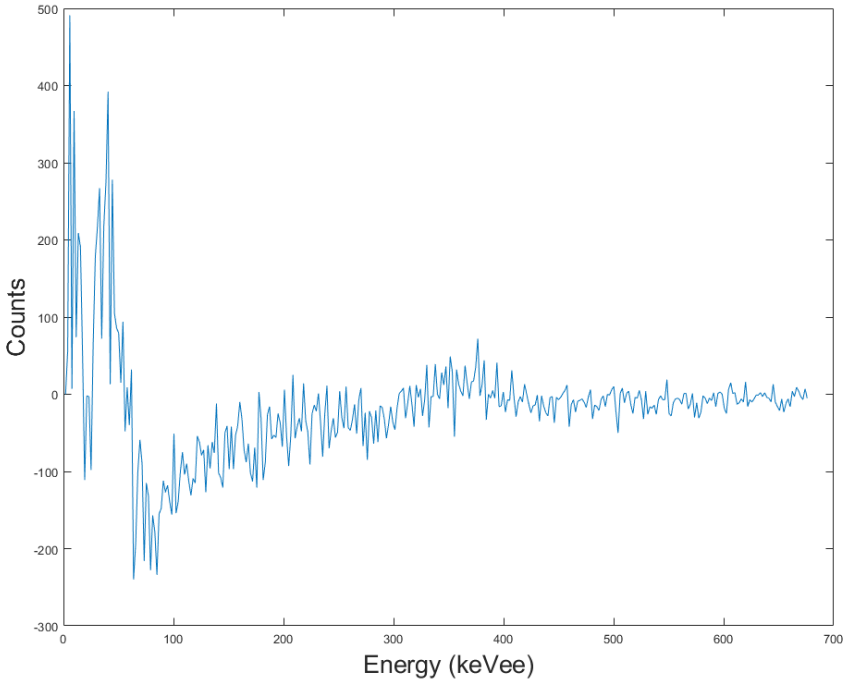

Figure 6. Top: subtracted spectra of pulse shape discrimination between thermalized neutrons and thermalized + absorbed neutrons. Bottom: neutron-associated region energy spectrum.

4. Conclusion

Lithium tetraborate ($Li_2B_4O_7$) is a low-Z but dense material that is particularly useful in the thermal neutron detection for its ability to convert 25 meV neutrons to alpha and triton particles. Based on literature precedents, lithium tetraborate nanoparticles were synthesized with a good monodispersity degree and were dispersed into fast n/γ discriminating plastic scintillators. MCNP simulations showed that a beneficial effect of plastic scintillation loading could be reached starting at 0.1 wt% of $Li_2B_4O_7$ added to the material. We succeeded in preparing a plastic scintillator with a concentration of 0.3 wt% of nanoparticles, albeit with a moderate light yield. The chemically-modified plastic scintillator then displayed numerous signatures: gamma counting, fast neutrons discrimination and two extra regions emanating from thermal neutrons captures, namely from ^{6}Li and ^{10}B nuclei.

Acknowledgements

The authors are indebted to the “Agence Nationale de la Recherche” for the grant allowed to CF, in the frame of the Nessyned project (ANR-15-CE39-0006). They also wish to thank Dr. Stéphane Normand for the loan of boron-loaded wood bricks.

References

1. G.H.V. Bertrand, M. Hamel, F. Sguerra, Current Status on Plastic Scintillators Modifications, Chem. – Eur. J., 20 (2014) 15660-15685.
2. G.H.V. Bertrand, M. Hamel, S. Normand, F. Sguerra, Pulse shape discrimination between (fast or thermal) neutrons and gamma rays with plastic scintillators: State of the art, Nucl. Instr. Methods A, 776 (2015) 114-128.
3. C.O. Muehlhause, G.E. Thomas, Slow Neutron Liquid Scintillation Detector, Phys. Rev., 85 (1952) 926.
4. Dumazert, R. Coulon, Q. Lecomte, G.H.V. Bertrand, M. Hamel, Gadolinium for neutron detection in current nuclear instrumentation research: A review, Nucl. Instr. Methods A, 882 (2018) 53-68.
5. J. Dumazert, R., Coulon, V., Kondrasovs, K. Boudergui, Compensation scheme for online neutron detection using a Gd-covered CdZnTe sensor, Nucl. Instr. Methods A, 857 (2017) 7-15.
6. M. Hamel, F. Carrel, Pseudo-gamma Spectrometry in Plastic Scintillators, in: A. Maghraby (Ed.) New Insights on Gamma Rays, InTech, 2017, pp. 47-66.
7. S.M. Carturan, T. Marchi, G. Maggioni, F. Gramegna, M. Degerlier, M. Cinausero, M.D. Palma, A. Quaranta, Thermal neutron detection by entrapping ^{6}LiF nanocrystals in siloxane scintillators, J. Phys.: Conf. Ser., 620 (2015) 012010.
8. S. Carturan, G. Maggioni, T. Marchi, F. Gramegna, M. Cinausero, A. Quaranta, M.D. Palma, ^{6}LiF oleic acid capped nanoparticles entrapment in siloxanes for thermal neutron detection, AIP Conf. Proc., 1753 (2016) 07005.
9. S.M. Carturan, M. Degerlier, G. Maggioni, T. Marchi, F. Gramegna, M. Cinausero, L. Stevanato, M. Vesco, A. Quaranta, Siloxane-Based Nanocomposites Containing ^{6}LiF Nanocrystals for Thermal Neutrons Detection, Acta Phys. Pol., A, 134 (2018) 405-408.
10. L. Singh, V., Chopra, S.P. Lochab, Synthesis and characterization of thermoluminescent $Li_2B_4O_7$ nanophosphor, J. Lumin., 131 (2011) 1177-1183.
11. D.M. Slaughter, C.R. Stuart, R.F. Klaass, D.B. Merrill, Performance of Large Neutron Detectors Containing Lithium-Gadolinium-Borate Scintillator, IEEE Trans. Nucl. Sci., 63 (2016) 1650-1658.
12. H.-J. Im, C. Willis, S. Saengkerdsub, R. Makote, M.D. Pawel, S. Dai, Scintillators for Alpha and Neutron Radiations Synthesized by Room Temperature Sol–Gel Processing, J. Sol-Gel Sci. Techn., 32 (2004) 117-123.
13. C. Frangville, A. Grabowski, J. Dumazert, E. Montbarbon, C. Lynde, R. Coulon, A. Venerosy, G.H.V. Bertrand, M. Hamel, Synthesis and evaluation of nanoparticles-loaded plastic scintillators aiming at discriminating fast neutrons, thermal neutrons and gamma rays, Mater. Chem. Front., (2019) DOI 10.1039/C9QM00222G.

14. D. Wolski, M. Moszynski, T. Ludziejewski, A. Johnson, W. Klamra, Ö. Skeppstedt, Comparison of n-γ discrimination by zero-crossing and digital charge comparison methods, Nucl. Instr. Methods A, 360 (1995) 584-592.

15. J.T. Goorley, MCNP6 User's Manual Version 1.0, Los Alamos National Laboratory (LANL), Los Alamos, NM (United States), LA-UR-13-22934 (2013).

16. P. Blanc, M. Hamel, L. Rocha, R.B. Pansu, F. Gobert, I. Lampre, S. Normand, Intrinsic Evaluation of n/γ Discrimination in Plastic Scintillators, IEEE Trans. Nucl. Sci., 61 (2014) 1995-2005.

17. J.F. Ziegler, J.P. Biersack, SRIM – The stopping and range of ions in matter (2010), Nucl. Instr. Methods B, 268 (2010), 1818-1823.

18. D.L. Horrocks, Interaction of Fission Fragments with Organic Scintillators, Rev. Sci. Instrum., 34 (1963) 1035-1040.

19. M. Ishii, Y. Kuwano, S. Asaba, T. Asai, M. Kawamura, N. Senguttuvan, T. Hayashi, M. Koboyashi, M. Nikl, S. Hosoya, K. Sakai, T. Adachi, T. Oku, H.M. Shimizu, Luminescence of doped lithium tetraborate single crystals and glass, Radiat. Meas., 38 (2004) 571–574.

20. M. Marseguerra, E. Padovani, S.A. Pozzi, Use of the MCNP-PoliMi code for time-correlation safeguards measurements, Prog. Nucl. Energy, 43 (2003) 305-311.

21. A. Mahl, H.A. Yemam, J. Stuntz, T. Remedes, A. Sellinger, U. Greife, Bis(pinacolato)diboron as an additive for the detection of thermal neutrons in plastic scintillators, Nucl. Instr. Methods A, 816 (2016) 96-100.